

Effective viscoelastic media for highly-heterogeneous saturated porous rocks

J. Germán Rubino, Claudia L. Ravazzoli* and Juan E. Santos*[†]*

ABSTRACT

Different theoretical and laboratory studies on the propagation of elastic waves in real rocks have shown that the presence of heterogeneities larger than the pore and grain sizes, but smaller than the predominant wavelengths (mesoscopic-scale heterogeneities) may produce significant effects in the attenuation and velocity dispersion of seismic waves. Such phenomenon is known as “mesoscopic effect” and is due to equilibration, via slow-wave diffusion, of wave-induced fluid pressure gradients. In this work, the effective complex P-wave and shear moduli of highly-heterogeneous fluid-saturated porous media are obtained by performing numerical *gedanken* experiments in a Montecarlo fashion, which allows to determine an effective viscoelastic medium by computing the moments of the associated phase velocities and inverse quality factors over a set of realizations. This numerical upscaling procedure involves the generation of a large number of realizations of synthetic representative bulk volumes, containing heterogeneities of different nature characterized by their spectral density distribution. The behavior of such rock samples is assumed to obey Biot’s equations, which are stated in the space-frequency domain with appropriate boundary conditions to simulate compressibility and shear tests. A finite-element method is used to obtain the solutions of the set of deterministic (local boundary-value) problems associated with each realization of the Montecarlo procedure. We present numerical examples showing the application of the proposed upscaling method and analyze the statistical properties of the phase velocities and inverse quality factors obtained for these kind of highly-heterogeneous fluid-saturated porous media.

INTRODUCTION

Seismic velocities and absorption properties of rocks are key-parameters in the characterization of their properties, and permit to obtain valuable information such as lithology, types of saturating fluids, physical state and degree of saturation. Consequently, the understanding of the physics controlling these parameters is of great interest for theoretical and exploration geophysics and other branches of science.

Recent studies (Pride, S.R. et al., 2004) suggest that the most important mechanism of attenuation in porous media is wave-induced fluid flow, which can take place at microscopic, macroscopic and mesoscopic spatial scales. The attenuation mechanism associated with wave-induced fluid flow at microscopic spatial scales is also known as *local fluid flow* or *squirt flow*, and is due to fluid-filled microcracks which respond with greater fluid-pressure changes than the main pore fluid producing fluid flow and, consequently, energy loss. This loss mechanism is able to explain ultrasonic attenuation data but is incapable of explaining the measured attenuation levels at seismic frequencies (Pride, S.R. et al., 2004).

The loss mechanism predicted by the theory of Biot (Biot, M.A., 1956a,b, 1962), the classical Biot's *global fluid flow* in homogeneous media, has a macroscopic nature and is due to wavelength-scale fluid pressure equilibration between the peaks and troughs of the fast propagating wave. This induces a relative displacement between the solid frame and the fluid, causing energy dissipation due to viscous friction. Although the attenuation due to global flow is generally important in the range of ultrasonic frequencies, it is not significant at the seismic frequency band.

The wave-induced fluid flow at *mesoscopic* scales takes place when a fast wave travels across an heterogeneous porous medium having inhomogeneities larger than the pore size but smaller than the predominant wavelengths. Basically, when a compressional wave squeezes an heterogeneous fluid-saturated porous material, the different regions of the medium, due to their distinct elastic properties, may undergo different strains and fluid pressures. This in turn produces fluid flow and Biot slow waves which diffuse away generating energy loss and velocity dispersion. These effects can also be produced by shear stresses applied to the medium, particularly when the mesoscopic heterogeneities have some local anisotropy associated with its shape (Mason, Y.J. and Pride, S.R., 2007). Recent results have demonstrated the importance of the mesoscopic effects in the context of exploration geophysics, being the dominant P-wave attenuation mechanism in reservoir rocks at seismic frequencies (Pride, S.R. et al. (2004)).

White and coauthors (White, J.E. et al., 1975; White, J.E., 1975) were the first to model the wave-induced fluid flow produced by mesoscopic-scale heterogeneities, showing that this mechanism can produce important attenuation and velocity dispersion effects at seismic frequencies in partially saturated rocks. They obtained approximated solutions of the response of porous layers alternately saturated with gas and water (White, J.E. et al., 1975) and of gas pockets in a water-saturated porous rock (White, J.E., 1975). Since then, many authors have made very important contributions to a better understanding of this subject. Some of them proposed other analytical models to explain the response of fluid-filled porous materials containing specific mesoscopic-scale heterogeneities. In this sense we can mention the work of Pride, S.R. and Berryman, J.G. (2003) who obtained an analytical model for the seismic response of a mixture of two different porous phases having a single dominant length scale. Other important contribution was due to Johnson, D.L. (2001), who developed an analytical solution for the case of patchy saturation, while Norris, A.N. (1993) and Gurevich, B. and Lopatnikov, S.L. (1995) focused on the case of layered porous media. The major drawback of these analytical theories is that they can only be used in the case of specific ideal heterogeneous rocks.

Mesoscopic effects have also been studied by performing numerical simulation of wave propagation, such as in Helle, H.B. et al. (2003) and Rubino, J.G. et al. (2007), among others. Unlike the before-mentioned analytical expressions this is a more versatile approach, since it allows to consider heterogeneities of any kind and shape. However, the use of extremely fine meshes needed to represent the inhomogeneities, and the fact that the seismic wave has to travel some wavelengths to evidence the mesoscopic effects makes this methodology computationally expensive or even not feasible. To overcome this limitation, a different and very interesting approach was recently presented by Mason, Y.J. and Pride, S.R. (2007). In their work, a time-varying stress is applied to the boundaries of an heterogeneous sample and by numerically computing the average stress and strain fields its effective complex moduli are determined.

Another important aspect that must be taken into account is that, at mesoscopic scales, rock parameter distributions are subject to uncertainty due to their high degree of spatial variability and the fact that direct observations are not possible. For this reason, many researchers dealing with mesoscopic-scale heterogeneities have represented the media using stochastic distributions of the rock parameters; for instance, Helle, H.B. et al. (2003) used the von Karman self-similar correlation function to model patchy fluid distributions, while Mason, Y.J. and Pride, S.R. (2007) analyzed the behavior of materials having local properties randomly sampled from certain probability distribution functions.

To analyze the effects of the spatial variability on the seismic response of these kind of media, it is very useful to perform Montecarlo simulation, which allows to consider multiple scenarios of the model. In this approach, a set of realizations of the stochastic parameters under consideration is generated, and for each realization a deterministic problem is solved to obtain the response of that sample. After a large number of realizations, the statistical moments of the computed variables are calculated and analyzed, giving the statistical behavior of the response of the medium.

With this idea, in this work we present a numerical upscaling procedure to obtain the *effective* complex P-wave and shear moduli of highly-heterogeneous fluid-saturated porous media and the corresponding effective phase velocities and inverse quality factors. The procedure consists in applying the Montecarlo simulation method to obtain the statistical properties of the response of a set of rock samples containing heterogeneities described by a given spectral density distribution. The numerical rock samples are subjected to time-harmonic compressibility and shear stresses, which permits to obtain (statistically) the effective complex moduli of the media. For each realization, the complex moduli are calculated by defining locally an *equivalent* viscoelastic solid having the same attenuation and velocity dispersion than the original fluid-saturated porous rock; for that purpose, *gedanken* experiments are set, which are defined as local boundary-value problems stated in the space-frequency domain on a representative sample of heterogeneous material. These numerical experiments are equivalent to oscillatory compressibility and shear tests. Biot's theory is used to model the response of the heterogeneous material to the applied stresses, and the approximate solution is obtained using a finite-element procedure.

We present numerical examples showing the application of the proposed methodology to obtain the effective complex P-wave and shear moduli, and their corresponding compressional and shear phase velocities and inverse quality factors, of highly-heterogeneous fluid-saturated porous media such as in the case of gas-water patchy saturation and rocks with mixtures of shale and sandstone.

REVIEW OF BIOT'S THEORY

The propagation of waves in a porous elastic solid saturated by a single-phase compressible viscous fluid was first analyzed by M.A. Biot in two important classical papers (Biot, M.A., 1956a,b). He considered a porous isotropic medium saturated by a single-phase, compressible viscous fluid, and assumed that due to deformation the fluid may flow relative to the solid frame causing viscous friction. Let $u^s = (u_i^s)$ and $\tilde{u}^f = (\tilde{u}_i^f)$, $i = 1, \dots, E$ denote the averaged displacement vectors of the solid and fluid phases, respectively, where E denotes

the Euclidean dimension. Also let

$$u^f = \phi(\tilde{u}^f - u^s), \quad (1)$$

be the average relative fluid displacement per unit volume of bulk material, where ϕ denotes the effective porosity. Set $u = (u^s, u^f)$ and note that

$$\xi = -\nabla \cdot u^f, \quad (2)$$

represents the change in fluid content.

Let $\varepsilon_{ij}(u^s)$ be the strain tensor of the solid phase. Also, let σ_{ij} , $i, j = 1, \dots, E$, and p_f denote the stress tensor of the bulk material and the fluid pressure, respectively. Following Biot, M.A. (1962), the elastic stress-strain relations can be written in the form:

$$\sigma_{ij}(u) = 2\mu \varepsilon_{ij}(u^s) + \delta_{ij}(\lambda_c \nabla \cdot u^s - \alpha K_{av} \xi), \quad (3)$$

$$p_f(u) = -\alpha K_{av} \nabla \cdot u^s + K_{av} \xi. \quad (4)$$

The coefficient μ is the shear modulus of the bulk material, considered to be equal to the shear modulus of the dry matrix. We also introduce

$$\lambda_c = K_c - \frac{2}{E}\mu, \quad (5)$$

where K_c is the undrained bulk modulus of the saturated (closed) material. Following Santos, J.E. et al. (1992) and Gassmann, F. (1951), the coefficients in (3) and (4) can be obtained from the relations

$$\alpha = 1 - \frac{K_m}{K_s}, \quad (6)$$

$$K_{av} = \left(\frac{\alpha - \phi}{K_s} + \frac{\phi}{K_f} \right)^{-1} \quad (7)$$

$$K_c = K_m + \alpha^2 K_{av}, \quad (8)$$

where K_s, K_m and K_f denote the bulk moduli of the solid grains, the dry matrix and the saturant fluid, respectively. The coefficient α is known as the effective stress coefficient of the bulk material. It is also convenient to introduce the undrained *plane-wave modulus* M_c , given by

$$M_c = \lambda_c + 2\mu. \quad (9)$$

For the present analysis, we consider that the moduli in the previous expressions are real and frequency independent.

The equations of motion

Let ρ_s and ρ_f denote the mass densities of the solid grains and the fluid and let

$$\rho_b = (1 - \phi)\rho_s + \phi\rho_f \quad (10)$$

denote the mass density of the bulk material. Let the positive definite matrix \mathcal{P} and the nonnegative matrix \mathcal{B} be defined by

$$\mathcal{P} = \begin{pmatrix} \rho_b I & \rho_f I \\ \rho_f I & gI \end{pmatrix}, \quad (11)$$

$$\mathcal{B} = \begin{pmatrix} I & 0I \\ 0I & bI \end{pmatrix}, \quad (12)$$

where I denotes the identity matrix in $\mathbb{R}^{E \times E}$. The mass coupling coefficient g represents the inertial effects associated with dynamic interactions between the solid and fluid phases, while the coefficient b includes the viscous coupling effects between such phases. They are given by the relations

$$b = \frac{\eta}{k}, \quad g = \frac{S\rho_f}{\phi}, \quad S = \frac{1}{2} \left(1 + \frac{1}{\phi} \right), \quad (13)$$

where η is the fluid viscosity and k the absolute permeability. The coefficient S is known as the structure or tortuosity factor, computed according to Berryman, J.G. (1982). Next, let $\mathcal{L}(u)$ be the second-order differential operator defined by

$$\mathcal{L}(u) = (\nabla \cdot \sigma(u), -\nabla p_f(u))^t. \quad (14)$$

Then, if $\omega = 2\pi f$ is the angular frequency, in the absence of body forces, the Biot's equations of motion stated in the space-frequency domain can be written in the form (Biot, M.A., 1956a,b)

$$-\omega^2 \mathcal{P}u(\mathbf{x}, \omega) + i\omega \mathcal{B}u(\mathbf{x}, \omega) - \mathcal{L}(u(\mathbf{x}, \omega)) = 0, \quad (15)$$

where \mathbf{x} denotes the position of an infinitesimal bulk volume in the Cartesian coordinate system. Considering the homogeneous case, it was shown by Biot, M.A. (1956a,b) that in these type of media two compressional waves, denoted here as P1 and P2, and one shear or S wave can propagate. The P1 and S waves correspond to the classical compressional and shear waves propagating in elastic or viscoelastic isotropic solids. The additional P2 slow mode is a wave strongly attenuated in the low frequency range, and it is associated with the motion out of phase of the solid and fluid. In terms of this theory, the physics of the mesoscopic attenuation and dispersion effects in heterogeneous porous media is basically the conversion from fast-waves energy into slow-wave energy at the discontinuities within the rock by means of a pressure diffusion process.

THE NUMERICAL *GEDANKEN* EXPERIMENTS

As we mentioned before, the numerical simulation of wave propagation can be used to study the mesoscopic effects that take place in highly-heterogeneous fluid-saturated porous media (Helle, H.B. et al., 2003; Rubino, J.G. et al., 2007). However, it is computationally expensive or even not feasible due to the extremely fine meshes that would be needed to define the mesoscopic-scale heterogeneities and to the fact that the waves should travel some wavelengths to evidence the mesoscopic effects.

A different and very convenient approach to achieve this goal is to perform numerical *gedanken* experiments: by applying time-harmonic compressional and shear stresses to porous saturated rocks, their *equivalent* complex P-wave and shear moduli are obtained by defining locally an equivalent viscoelastic medium having the same attenuation and velocity dispersion than the original porous rock. The theoretical basis for this procedure were given in the works of White, J.E. et al. (1975); Dutta, N.C. and Odé, H. (1979) and Johnson, D.L. (2001).

The idea is illustrated in Figure 1, which shows a schematic representation of an undrained oscillatory compressibility test. In this experiment the sample is subjected to a time-harmonic compression with constant amplitude of the form $\Delta P e^{i\omega t}$ on its top boundary, and no tangential forces are applied on the boundaries of the sample. Also, the solid is not allowed neither to move on the bottom boundary nor have horizontal displacements on the lateral boundaries, and the fluid is not allowed to flow into or out of the sample.

Denoting by V the original volume of the sample, its (complex) oscillatory volume change, $\Delta V(\omega)$, allows us to define the *equivalent* undrained complex P-wave modulus $\overline{M}_c(\omega)$, by using the relation

$$\frac{\Delta V(\omega)}{V} = -\frac{\Delta P}{\overline{M}_c(\omega)}, \quad (16)$$

valid for a viscoelastic homogeneous medium in the quasistatic case.

In order to estimate this volume change, Biot's equations of motion (15) are solved under proper boundary conditions. In this sense, let $\Omega = (0, L)^2$ be a domain in the (x, y) -plane representing the rock sample to be compressed in the test. Set Γ the boundary of Ω , given by $\Gamma = \Gamma^L \cup \Gamma^B \cup \Gamma^R \cup \Gamma^T$, where

$$\begin{aligned} \Gamma^L &= \{(x, y) \in \Gamma : x = 0\}, & \Gamma^R &= \{(x, y) \in \Gamma : x = L\}, \\ \Gamma^B &= \{(x, y) \in \Gamma : y = 0\}, & \Gamma^T &= \{(x, y) \in \Gamma : y = L\}. \end{aligned}$$

Also, denote by ν the unit outer normal on Γ and let χ be a unit tangent on Γ so that $\{\nu, \chi\}$ is an orthonormal system on Γ . Then, to estimate the volume change $\Delta V(\omega)$, we consider the solution of (15) under the following boundary conditions

$$\begin{aligned} \sigma(u)\nu &= (0, -\Delta P), & (x, y) &\in \Gamma^T, \\ \sigma(u)\nu \cdot \chi &= 0, & (x, y) &\in \Gamma^L \cup \Gamma^R, \\ u^s \cdot \nu &= 0, & (x, y) &\in \Gamma^L \cup \Gamma^R, \\ u^s &= 0, & (x, y) &\in \Gamma^B, \\ u^f \cdot \nu &= 0, & (x, y) &\in \Gamma, \end{aligned} \quad (17)$$

where the factor $e^{i\omega t}$ is omitted from now on, since the problem is formulated in the space-frequency domain.

The vertical displacements $u_2^s(x, L, \omega)$ on Γ^T allow us to obtain an average vertical displacement $u_2^{s,T}(\omega)$ suffered by the boundary Γ^T . Then, for each frequency ω , the volume change produced by the compressibility test can be approximated by $\Delta V(\omega) \approx L u_2^{s,T}(\omega)$, which enable us to compute the equivalent complex plane-wave modulus $\overline{M}_c(\omega)$ by using the relation (16). The corresponding complex compressional velocity is given by

$$V_{pc}(\omega) = \sqrt{\frac{\overline{M}_c(\omega)}{\overline{\rho}_b}}, \quad (18)$$

where $\overline{\rho}_b$ is the average bulk density of the rock sample. The following relations allow us to estimate the equivalent compressional phase velocity $V_p(\omega)$ and (inverse) quality factor

$Q_p(\omega)$ in the form:

$$V_p(\omega) = \left[\operatorname{Re} \left(\frac{1}{V_{pc}(\omega)} \right) \right]^{-1}, \quad (19)$$

$$\frac{1}{Q_p(\omega)} = \frac{\operatorname{Im}(V_{pc}(\omega)^2)}{\operatorname{Re}(V_{pc}(\omega)^2)}. \quad (20)$$

Following the same methodology, to obtain the *equivalent* complex shear modulus of the fluid-saturated porous medium, let us consider the solution of (15) under the following boundary conditions

$$\begin{aligned} \sigma(u)\nu &= g(x, y), \quad (x, y) \in \Gamma^T \cup \Gamma^L \cup \Gamma^R, \\ u^s &= 0, \quad (x, y) \in \Gamma^B, \\ u^f \cdot \nu &= 0, \quad (x, y) \in \Gamma, \end{aligned} \quad (21)$$

where

$$g(x, y) = \begin{cases} (0, -\Delta T), & (x, y) \in \Gamma^L, \\ (0, \Delta T), & (x, y) \in \Gamma^R, \\ (\Delta T, 0), & (x, y) \in \Gamma^T, \end{cases} \quad (22)$$

and ΔT denotes the constant amplitude of the external oscillatory stress. This boundary-value problem is the mathematical representation of a shear experiment as shown in Figure 2, where the solid is not allowed to move on Γ^B , the fluid is not allowed to flow into or out of the sample and shear stresses are applied on the boundaries Γ^L , Γ^R and Γ^T .

The change in shape of the rock sample allows to recover its *equivalent* complex shear modulus $\bar{\mu}_c(\omega)$ by using the relation

$$tg(\theta(\omega)) = \frac{\Delta T}{\bar{\mu}_c(\omega)}, \quad (23)$$

where $\theta(\omega)$ is the departure angle between the original positions of the lateral boundaries and those after applying the shear stresses (see, for example, Kolsky, H. (1963)). Equation (23) holds for this experiment in a viscoelastic homogeneous media in the quasistatic approximation.

The horizontal displacements $u_1^s(x, L, \omega)$ at the top boundary Γ^T allow us to obtain, for each frequency, an average horizontal displacement $u_1^{s,T}(\omega)$ suffered by the boundary Γ^T . This average value allows us to approximate the change in shape suffered by the sample, given by $tg(\theta(\omega)) = u_1^{s,T}(\omega)/L$, which from (23) let us estimate $\bar{\mu}_c(\omega)$. The complex shear velocity is given by $V_{sc}(\omega) = \sqrt{\frac{\bar{\mu}_c(\omega)}{\rho_b}}$ and the equivalent shear phase velocity $V_s(\omega)$ and (inverse) quality factor $Q_s(\omega)$ are estimated using the relations

$$V_s(\omega) = \left[\operatorname{Re} \left(\frac{1}{V_{sc}(\omega)} \right) \right]^{-1}, \quad (24)$$

$$\frac{1}{Q_s(\omega)} = \frac{\operatorname{Im}(V_{sc}(\omega)^2)}{\operatorname{Re}(V_{sc}(\omega)^2)}. \quad (25)$$

Numerical approximation

In order to obtain the equivalent complex moduli of a given rock sample, we approximate the solution of the equations of motion (15) under the boundary conditions (17) or (21) using a finite-element procedure. With this objective, let us introduce some notation to state a variational formulation for (15) and either (17) or (21). For $X \subset \mathbb{R}^E$ with boundary ∂X , let $(\cdot, \cdot)_X$ and $\langle \cdot, \cdot \rangle_{\partial X}$ denote the complex $L^2(X)$ and $L^2(\partial X)$ inner products for scalar, vector, or matrix valued functions. In addition, if $X = \Omega$ or $X = \Gamma$, the subscript X may be omitted such that $(\cdot, \cdot) = (\cdot, \cdot)_\Omega$ or $\langle \cdot, \cdot \rangle = \langle \cdot, \cdot \rangle_\Gamma$. Also, let us introduce the spaces

$$H_{0,B}^{1,P}(\Omega) = \{v \in (H^1(\Omega))^2 : v \cdot \nu = 0 \text{ on } \Gamma^L \cup \Gamma^R, v = 0 \text{ on } \Gamma^B\},$$

$$H_{0,B}^{1,T}(\Omega) = \{v \in (H^1(\Omega))^2 : v = 0 \text{ on } \Gamma^B\},$$

$$H_0(\text{div}; \Omega) = \{v \in [L^2(\Omega)]^2 : \nabla \cdot v \in L^2(\Omega), v \cdot \nu = 0, \text{ on } \Gamma\}.$$

Let us introduce the spaces

$$\mathcal{V}^{(P)} = \left[H_{0,B}^{1,P}(\Omega) \right]^2 \times H_0(\text{div}; \Omega), \quad \mathcal{V}^{(T)} = \left[H_{0,B}^{1,T}(\Omega) \right]^2 \times H_0(\text{div}; \Omega).$$

Then, for the compressional experiment multiply equation (15) by $v = (v^s, v^f)^t \in \mathcal{V}^{(P)}$, use integration by parts and apply the boundary conditions (17) to see that the solution $u^{(P)} = (u^{(s,P)}, u^{(f,P)}) \in \mathcal{V}^{(P)}$ of (15) and (17) satisfies *the weak form*:

$$\Lambda(u^{(P)}, v) = \langle \Delta p, v^s \cdot \nu \rangle_{\Gamma^T}, \quad \text{for all } v = (v^s, v^f)^t \in \mathcal{V}^{(P)}, \quad (26)$$

where for $u = (u^s, u^f), v = (v^s, v^f) \in [H^1(\Omega)]^2 \times H(\text{div}; \Omega)$, the bilinear form $\Lambda(u, v)$ is defined by

$$\Lambda(u, v) = -\omega^2 (\mathcal{P}u, v) + i\omega (\mathcal{B}u, v) + \sum_{l,m} (\tau_{lm}(u), \varepsilon_{lm}(v^s)) - (p_f(u), \nabla \cdot v^f).$$

Similarly, the solution $u^{(T)} = (u^{(s,T)}, u^{(f,T)}) \in \mathcal{V}^{(T)}$ of (15) and (21) satisfies *the weak form*:

$$\Lambda(u^{(T)}, v) = \langle g, v^s \rangle_{\Gamma \setminus \Gamma^B}, \quad \text{for all } v = (v^s, v^f)^t \in \mathcal{V}^{(S)}. \quad (27)$$

A functional analysis argument involving Korn's second inequality (Duvaut, G. and Lions, J.L., 1976; Nitsche, 1981; Ciarlet, 1978) shows that uniqueness holds for problems (26) and (27) for $\omega > 0$ and sufficiently small. More specifically, setting

$$\mathbf{E} = \begin{pmatrix} \lambda_c + 2\mu & \lambda_c & 0 \\ \lambda_c & \lambda_c + 2\mu & 0 \\ 0 & 0 & 2\mu \end{pmatrix},$$

ω must satisfy the inequality:

$$\omega < \frac{1}{C_1} \sqrt{\frac{\lambda_{\min}(\mathbf{E})}{\rho_b^{\max}}}, \quad (28)$$

where ρ_b^{max} denotes the maximum value of the bulk density and $\lambda_{min}(\mathbf{E})$ is the minimum eigenvalue of the matrix \mathbf{E} . Also, C_1 is a constant associated with Korn's second inequality (Santos et al., to appear). Existence for (26) and (27) will be assumed.

In order to approximate the displacements $u^{(P)}$ and $u^{(T)}$, we consider a non-overlapping partition of Ω , $\mathcal{T}^h(\Omega)$, into squares Ω_j , $j = 1, 2, \dots, J$ of side length h . Two different finite-element spaces, denoted $\mathcal{N}_{0,B}^{h,P}$ and $\mathcal{N}_{0,B}^{h,T}$ are used to approximate the solid displacement vector for the compressibility and shear tests, respectively. They are defined as follows

$$\begin{aligned}\mathcal{N}_{0,B}^{h,P} &= \{v : v|_{\Omega_j} \in P_{1,1} \times P_{1,1}, v \cdot \nu = 0 \text{ on } \Gamma^L \cup \Gamma^R, v = 0 \text{ on } \Gamma^B\} \cap [C^0(\bar{\Omega})]^2, \\ \mathcal{N}_{0,B}^{h,T} &= \{v : v|_{\Omega_j} \in P_{1,1} \times P_{1,1}, v = 0 \text{ on } \Gamma^B\} \cap [C^0(\bar{\Omega})]^2,\end{aligned}$$

where $P_{1,1}$ denotes the polynomials of degree not greater than 1 on each variable.

To approximate the fluid displacement a closed subspace of the vector part of the Raviart-Thomas-Nedelec space of zero order, denoted \mathcal{W}_0^h , is employed (Raviart, P.A. and Thomas, J.M. (1975); Nedelec, J.C. (1980)). It is defined as

$$\mathcal{W}_0^h = \{v : v|_{\Omega_j} \in P_{1,0} \times P_{0,1}, v \cdot \nu = 0, \text{ on } \Gamma\}.$$

Figure 3 shows the local degrees of freedom (*dofs*) associated with each component of the solid and the fluid displacement vectors.

Let us define the finite-element spaces

$$\mathcal{V}^{(h,P)} = \mathcal{N}_{0,B}^{h,P} \times \mathcal{W}_0^h, \quad \mathcal{V}^{(h,T)} = \mathcal{N}_{0,B}^{h,T} \times \mathcal{W}_0^h.$$

Then, the finite-element procedure to compute the approximate solution of the compressibility problem (26) is defined as follows: find $u^{(h,P)} = (u^{(s,h,P)}, u^{(f,h,P)})^t \in \mathcal{V}^{h,P}$ such that

$$\Lambda(u^{(h,P)}, v) = \langle \Delta p, v^s \cdot \nu \rangle_{\Gamma^T}, \quad v = (v^s, v^f)^t \in \mathcal{V}^{(h,P)}. \quad (29)$$

Similarly, the finite-element procedure to compute the approximate solution of the shear problem (27) is: find $u^{(h,T)} = (u^{(s,h,T)}, u^{(f,h,T)})^t \in \mathcal{V}^{(h,T)}$ such that

$$\Lambda(u^{(h,T)}, v) = \langle g, v^s \rangle_{\Gamma \setminus \Gamma_B}, \quad v = (v^s, v^f)^t \in \mathcal{V}^{(h,T)}. \quad (30)$$

Uniqueness for the solution of (29) and (30) can be demonstrated with the same argument than for the continuous problems (26) and (27). Existence follows from finite dimensionality. It can be shown that the error associated with the finite-element problems (29) and (30) measured in the energy norm is of order h (Santos et al., to appear).

To validate the procedure to estimate the P-wave modulus, we assume that the domain Ω is composed of two poroelastic layers of equal thickness 0.2 m, one fully saturated with water and the other fully saturated with gas. The physical properties of the solid matrix are taken constant in all the domain, and correspond to the sandstone 1 in Table 1, while the physical properties of the fluids (water and gas) are given in Table 2. The physical properties of the solid grains and those of the fluids were taken from Carcione, J.M. and Picotti, S.

(2006); in addition, following their work, the bulk and shear moduli of the dry matrices were computed using the model of Krief, M. et al. (1990), while the Kozeny-Carman relation was employed to relate porosity and permeability.

Next, we compare the phase velocities and inverse quality factors obtained using our numerical approach for 15 frequencies between 0 and 100 Hz with the corresponding values obtained using the analytical theory of White, J.E. (1975) but, in the last case, considering a periodic medium composed of alternating layers of equal thickness 0.4 m saturated with either gas or water. This comparison is valid because the boundary conditions (17) for the compressibility test can be associated with a compression similar to that proposed by White, J.E. (1975), but applied to a periodic sample obtained by a mirror reflection with respect to the x-axis of the domain Ω .

Figures 4 and 5 display the P-wave phase velocities and inverse quality factors, respectively, obtained with the compressibility test (dots) and with the White's theory (line), where in both cases an excellent matching between the two approaches can be observed. Moreover, the position of the peak in the curve of $\frac{1}{Q_p}$ is in good agreement with the theoretical predictions obtained using concepts from standard diffusion and wave propagation theories (Mavko, G. et al., 1998; Dutta, N.C. and Odé, H., 1979).

To validate the procedure for the estimation of the shear modulus, we suppose that the domain Ω is composed of two horizontal layers L_1 and L_2 , of thicknesses T_1 and T_2 respectively, such that $T_1 + T_2 = 1$ m. We assume that both layers are saturated with water but their solid matrices are different: the solid matrix of the layer L_1 is the sandstone 1 while the solid matrix of the layer L_2 is shale, with the physical parameters given in Table 1.

Figure 6 displays the equivalent shear modulus obtained with the shear test (with points) for different values of the shale content $T_2/(T_1 + T_2)$ and in the zero-limit frequency. As it can be seen, we found that these values are in excellent agreement with the shear modulus obtained using the Reuss average for an effective mixture of sand and shale (Mavko, G. et al., 1998). As expected, the imaginary part of the modulus is negligible due to the low frequency used in this experiment.

A MONTECARLO APPROACH TO OBTAIN THE EFFECTIVE COMPLEX MODULI

The compressibility and shear tests defined in the previous section allow to numerically estimate the equivalent complex moduli of rock samples when the spatial distribution of their properties is known in detail. However, as we mentioned before, a precise knowledge of the spatial distribution of the rock heterogeneities at mesoscopic scales may not be feasible. Instead, they can be represented as stochastic functions (parameters) with given spectral density distributions. In this sense, to obtain significant values for the *effective* complex moduli in highly-heterogeneous fluid-saturated porous media, we propose to apply the numerical *gedanken* experiments in a Montecarlo fashion. Thus, the compressibility and shear tests are applied to representative volumes of bulk material containing stochastic heterogeneities characterized by fractal spectral density distributions, and the boundary-value problems are solved for each realization. The means and variances of the phase velocities and inverse quality factors associated with the complex moduli are obtained by averaging over realizations of the stochastic parameters, and they represent the statistical

behavior of the response of the porous rocks under consideration.

The size of the representative volume, i.e. the computational domain to be used in the numerical experiments, is not arbitrary: the side length L has to be big enough to contain a significant number of mesoscopic-scale heterogeneities but, at the same time, it has to be much smaller than the wavelengths associated to each excitation frequency. To find an upper bound for L we check that the compressibility and shear tests applied to homogeneous samples of side length L , composed of any of the different materials forming the heterogeneous medium, give negligible attenuation and velocity dispersion in the frequency range under consideration.

The solution of the numerical problem (15) under the respective boundary conditions (Eq. (17) or (21)) is approximated using the finite-element procedure explained in the previous section for different samples for a number of frequencies ω_m , $m = 1, \dots, N_F$, from which the values of $V_p^n(\omega_m)$, $V_s^n(\omega_m)$, $1/Q_p^n(\omega_m)$ and $1/Q_s^n(\omega_m)$ are obtained for the n^{th} realization. This procedure is repeated for a large number of realizations $n = 1, \dots, N_R$, and the statistical behavior of the phase velocities and inverse quality factors is analyzed by computing the means and variances of these quantities in the form:

$$\langle \beta(\omega_m, N_R) \rangle = \frac{1}{N_R} \sum_{n=1}^{N_R} \beta^n(\omega_m), \quad \beta = V_p, 1/Q_p, V_s, 1/Q_s, \quad (31)$$

$$\sigma_\beta^2(\omega_m, N_R) = \frac{1}{(N_R - 1)} \sum_{n=1}^{N_R} [\beta^n(\omega_m) - \langle \beta(\omega_m, N_R) \rangle]^2. \quad (32)$$

To analyze the convergence of the Montecarlo approach in terms of the number of realizations N_R , the frequency average of the variances are computed by

$$\| \sigma_\beta^2(N_R) \| = \left[\frac{1}{N_F} \sum_{m=1}^{N_F} \sigma_\beta^2(\omega_m, N_R) \right]^{1/2}, \quad \beta = V_p, V_s, 1/Q_p, 1/Q_s. \quad (33)$$

Following the criterion used by Guarracino, L. and Santos, J. E. (2004), the Montecarlo simulations are stopped after N_R^* realizations, such that the variances (33) of the computed quantities stabilize at constant values. Then, the averages $\langle \beta(\omega_m, N_R^*) \rangle$ are our *effective* velocities and inverse quality factors of the heterogeneous fluid-saturated poroelastic material.

NUMERICAL EXAMPLES

To illustrate the application of the proposed methodology to obtain the effective viscoelastic properties of highly-heterogeneous fluid-saturated porous media, we show some numerical examples in the case of patchy gas-water saturation and for a composite water-saturated medium whose rock matrix is a mixture of shale and sandstone.

The patchy gas-water saturation case

A very interesting case may arise in hydrocarbon reservoirs, where regions of non-uniform patchy saturation may occur at the transition zones between gas and water. Such patchy-

saturation patterns induce important mesoscopic attenuation effects in the seismic band of frequencies, as shown by White, J.E. (1975).

In order to study and quantify these effects, we consider a poroelastic sample with a spatially variable gas-water distribution in the form of irregular patches fully saturated with gas and zones fully saturated with water. No mixing nor capillary forces are taken into account and the two fluids are assumed to occupy different mesoscopic regions of the model. To generate these kind of heterogeneities we use a stochastic fractal field based on the so-called von Karman self-similar correlation functions. Following Frankel, A. and Clayton, R.W. (1986) and more recently Santos, J.E. et al. (2005), we consider a particular case for which the spectral density of the stochastic field is given by:

$$S_d(k_x, k_y) = S_0(1 + k^2 a^2)^{-(H+E/2)} \quad (34)$$

where $k = \sqrt{k_x^2 + k_y^2}$ is the radial wavenumber, a the correlation length, H is a self-similarity coefficient ($0 < H < 1$) and S_0 is a normalization constant. Equation (34) corresponds to a fractal process of dimension $D = E + 1 - H$ at scales smaller than a .

The first step to generate a patchy fluid distribution is to assign to each subdomain Ω_j of the partition \mathcal{T}^h a pseudo-random number using a generator with uniform distribution associated to a given *seed* number. This random field is Fourier transformed to the spatial wavenumber domain and its amplitude spectrum is filtered using equation (34). The result is then transformed back to the spatial domain, obtaining a micro-heterogeneous water saturation model $S_w^{(j)}$, $j = 1, \dots, J$. Next, to assign to each Ω_j either pure water or pure gas, we choose a value S_w^* so that, for each cell Ω_j where $S_w^{(j)} \leq S_w^*$, then Ω_j is changed to full gas saturation, while if $S_w^{(j)} > S_w^*$ then Ω_j is changed to full water saturation. For this patchy-saturation model we compute an overall water saturation \bar{S}_w with a corresponding overall gas saturation $1 - \bar{S}_w$.

For this example, we consider that Ω is a square domain of side length $L = 0.5$ m, and the partition \mathcal{T}^h is composed of $J = 75 \times 75$ squares of side length $h = 0.5/75$ m. The parameters of the fractal spectral density are respectively $E = 2$, $D = 2.2$, $a = 0.1$ m. For each realization, the excitation frequency is varied from 0 to 100 Hz using $N_F = 15$ equally spaced values. The physical properties of the solid matrix are taken constant in the domain, and correspond to the sandstone 1 of Table 1, while the physical parameters of the fluids are those given in Table 2.

We analyze a set of experiments involving $N_R = 70$ realizations, choosing S_w^* in each case so that the overall gas saturation in each realization is fixed and equal to 0.1. An example of the gas-water distribution for a particular realization is illustrated in Figure 7, where the black zones correspond to pure gas saturation and the white ones to pure water saturation.

Let us analyze the induced fluid pressure field for the particular fluid distribution displayed in Figure 7. This is shown in Figure 8, where we plot the normalized fluid-pressure amplitude produced by the compressibility experiment at a frequency of 50 Hz. It should be remarked that, despite the fact that the volume change in the gas-saturated zones is greater than in the water-saturated ones, the fluid pressures induced in the water patches are greater than in the gas patches. This effect can be understood by analyzing (4), and taking into account that the bulk modulus of the gas is much smaller than that of the

water, and consequently (from (7)), the same holds for K_{av} . The associated fluid-pressure gradient, which has its maximum values at the boundaries between the gas-saturated zones and the water-saturated ones, produces fluid flow and Biot slow waves which diffuse away from the interfaces generating energy losses and velocity dispersion.

Next, we analyze the Montecarlo procedure to obtain the effective complex moduli, velocities and quality factors for the patchy-saturation distributions, as described in the previous section. Figure 9 shows the variance of the compressional phase velocity averaged over the whole range of frequencies for different values of the number of realizations N_R , where it can be seen that after 70 realizations this parameter stabilizes at a very low constant value. The variance of the compressional inverse quality factor presents a similar trend, and is not included here for brevity. These results suggest that the effective compressional phase velocity and inverse quality factor are representative parameters for the kind of media and overall saturation under consideration.

Figure 10 displays the effective compressional phase velocity versus frequency (after 70 realizations) and its corresponding standard deviation interval (indicated with dotted lines). We observe an important increasing dispersion of the phase velocity with frequency within the seismic range.

Figure 11 shows the behavior of the effective compressional inverse quality factor versus frequency and its corresponding standard deviation. Note the very high mesoscopic attenuation levels in almost all the frequency range under consideration, with a minimum Q_p value on the order of 12 at 40 Hz. These results show the drastic amplitude losses that would suffer compressional waves propagating through these kind of media. In this context, it can be remarked that for these fractal-type distributions, because of the different scales of heterogeneity involved, it is very difficult to predict theoretically the existence of an attenuation peak in the frequency range analyzed. For a general analysis on this subject see Johnson, D.L. (2001).

In order to obtain the effective complex shear modulus of these samples we also performed the shear tests to the same set of realizations of the patchy-saturated rocks. As expected, the effective shear modulus resulted to have negligible imaginary part, while its real part was very close to the shear modulus of the dry matrix. This behavior is due to the fact that shear tests applied to samples where the heterogeneities are related to fluid inhomogeneities induce negligible values of fluid-pressure gradient and consequently negligible mesoscopic effects.

The shale-sandstone mixture case

Mesoscopic effects can also be created by mesoscopic-scale heterogeneities associated with the lithology of the rock. In this example, we analyze the response of rocks composed of a mixture of two different materials: the sandstone 2 of Table 1 and shale (with properties given in the same Table), fully saturated with water. We consider that the domain Ω is a square of side length $L = 0.07$ m, and the partition \mathcal{T}^h is composed of 75×75 squares Ω_j of equal side length. For each realization, the excitation frequency is varied from 0 to 100 Hz using $N_F = 15$ equally spaced values.

As in the previous example, we assume that the irregular distribution of shale and sandstone can be represented using the stochastic fractal field associated to the von Karman

spectral density (34). The procedure to generate the binary distribution is completely analogous to that we used to create the patchy gas-water distributions, from which we obtain a micro-heterogeneous sandstone content model $S^{(j)}, j = 1, \dots, J$. Next, to assign to the porous matrix of each Ω_j either pure shale or pure sandstone, we choose a value S^* so that for each subdomain Ω_j where $S^{(j)} \leq S^*$ the rock matrix is changed to pure shale, while if $S^{(j)} > S^*$ the matrix is changed to pure sandstone. In this way, the heterogeneous mixture model is constructed with a resulting overall sandstone content \bar{S} for the computational rock sample.

We consider again a set of experiments involving $N_R = 70$ realizations, choosing S^* in each case so that the overall sandstone content \bar{S} of each realization is fixed and equal to 0.5. The parameters of the fractal spectral density are respectively $E = 2$, $D = 2.2$, and the correlation length a is taken to be 0.0005 m. An example of the distribution of shale and sandstone for a given realization is illustrated in Figure 12, where the black zones correspond to pure shale while the white ones to pure sandstone.

To quantify the mesoscopic effects associated with these kind of media, we apply the Montecarlo procedure to obtain the phase velocities and inverse quality factors associated with the effective complex moduli. We checked that the variances of both the shear and compressional velocities and inverse quality factors stabilized at constant values after 70 realizations.

These lithological variations produce non-negligible mesoscopic effects in the case of the compressibility tests, as it is shown in Figure 13, where the effective compressional inverse quality factor is plotted as a function of the frequency (solid lines); we can see that for frequencies around 40 Hz the quality factor Q_p is about 70. The associated compressional phase velocity shows very slight dispersion, with an increase of 2 % between 0 and 100 Hz; the corresponding Figure is not included for brevity.

These mesoscopic-scale heterogeneities also produce non-negligible pressure gradients in the case of the shear test. This is illustrated in Figure 14 where we plot the normalized fluid-pressure amplitude for a frequency of 20 Hz for the particular realization shown in Figure 12. It can be seen that the applied shear stresses induce fluid-pressure gradients, also causing energy losses and velocity dispersion. This can be appreciated in Figure 15 where we plot the effective shear inverse quality factor as function of the frequency (solid lines) and its corresponding standard deviation (dotted lines). It can be seen that the lithological variations produce non-negligible attenuation effects, with values of Q_s of about 75 for frequencies around 25 Hz. This result demonstrates that shear waves propagating through these kind of media are also affected by wave-induced fluid flow effects. The associated effective shear phase velocity shows very slight dispersion, with a 1.5 % increase between 0 and 100 Hz; also in this case we do not include the corresponding Figure for brevity.

CONCLUSIONS

In this paper we presented a numerical upscaling procedure to obtain the effective complex P-wave and shear moduli of highly-heterogeneous fluid-saturated porous media. The methodology is based on a finite-element solution of the classical Biot's equations in the space-frequency domain to simulate oscillatory compressibility and shear tests to obtain the equivalent complex undrained plane-wave and shear moduli and the corresponding phase

velocities and quality factors of a given heterogeneous sample. The effective viscoelastic medium is defined in a Montecarlo fashion by computing the moments of the equivalent phase velocities and inverse quality factors over a set of realizations of the stochastic rock parameters with a given spectral density distribution. Unlike published theoretical works for ideal geometries, our method allows to simulate any kind of heterogeneities within the domain.

In order to illustrate the procedure, numerical experiments were performed to obtain the effective complex moduli of gas-water patchy-saturated sandstones and of water-saturated mixtures of sandstone and shale for frequencies lying between 0 and 100 Hz. We verified that the mesoscopic attenuation and velocity dispersion can be very important in the case of compressional waves propagating in patchy-saturated media. Also, we showed that mesoscopic-scale lithological variations can produce non-negligible mesoscopic effects in the propagation of shear and compressional waves. Although we focused our attention in the seismic range of frequencies, these experiments can also be performed at higher frequencies, as long as the domain size and heterogeneity scales are properly chosen.

The proposed numerical upscaling procedure can be used to replace a Biot medium containing mesoscopic-scale heterogeneities characterized by a given spectral density distribution by an effective viscoelastic solid where the mesoscopic effects are included by solving a set of local boundary-value problems. This methodology is particularly important in the context of exploration geophysics, since performing numerical simulation of wave propagation employing the viscoelastic equation is computationally less expensive than any numerical procedure based on the discretization of the full Biot's equations for the same order of accuracy. This subject will be investigated in future works.

ACKNOWLEDGMENTS

This work was partially financed by the Agencia Nacional de Promoción Científica y Tecnológica, Argentina (PICT 03-13376) and by CONICET (PIP 04-5126).

REFERENCES

- Berryman, J.G., 1982, Elastic waves in fluid-saturated porous media: in *Lecture Notes in Physics*. Springer Verlag, Berlin, 38–50.
- Biot, M.A., 1956a, Theory of propagation of elastic waves in a fluid-saturated porous solid. i. low frequency range: *J. Acoust. Soc. Am.*, **28**, 168–171.
- , 1956b, Theory of propagation of elastic waves in a fluid-saturated porous solid. ii. high frequency range: *J. Acoust. Soc. Am.*, **28**, 179–191.
- , 1962, Mechanics of deformation and acoustic propagation in porous media: *J. Appl. Phys.*, **33**, 1482–1498.
- Carcione, J.M. and Picotti, S., 2006, P-wave seismic attenuation by slow-wave diffusion: Effects of inhomogeneous rock properties: *Geophysics*, **71** No3, O1–O8.
- Ciarlet, P., 1978, *The finite element method for elliptic equations*: North-Holland.
- Dutta, N.C. and Odé, H., 1979, Attenuation and dispersion of compressional waves in fluid-filled porous rocks with partial gas saturation (white model). part i: Biot theory: *Geophysics*, **44** No 11, 1777–1788.

- Duvaut, G. and Lions, J.L., 1976, *Inequalities in mechanics and physics*: Springer Verlag, Berlin.
- Frankel, A. and Clayton, R.W., 1986, Finite difference simulation of seismic wave scattering: implications for the propagation of short period seismic waves in the crust and models of crustal heterogeneity: *J. Geophys. Res.*, **91**, 6465–6489.
- Gassmann, F., 1951, Über die elastizität poroser medien (on the elasticity of porous media): *Vierteljahrsschrift der Naturforschenden Gessellschaft in Zurich*, **96**, 1–23.
- Guarracino, L. and Santos, J. E., 2004, Stochastic modelling of variable saturated transient flow in fractal porous media: *Mathematical Geology*, **36**, 217–238.
- Gurevich, B. and Lopatnikov, S.L., 1995, Velocity and attenuation of elastic waves in finely layered porous rocks: *Geophys. J. Int.*, **121**, 933–947.
- Helle, H.B., Pham, N.M., and Carcione, J.M., 2003, Velocity and attenuation in partially saturated rocks: poroelastic numerical experiments: *Geophysical Prospecting*, **51**, 551–566.
- Johnson, D.L., 2001, Theory of frequency dependent acoustics in patchy-saturated porous media: *J. Acoust. Soc. Am.*, **110**, 682–694.
- Kolsky, H., 1963, *Stress waves in solids*: Dover Publications.
- Krief, M., Garat, J., Stellingwerff, J., and Ventre, J., 1990, A petrophysical interpretation using the velocities of p and s waves (full waveform sonic): *The Log Analyst*, **31**, 355–369.
- Mason, Y.J. and Pride, S.R., 2007, Poroelastic finite difference modelling of seismic attenuation and dispersion due to mesoscopic-scale heterogeneity: *Journal of Geophysical Research*, **112**, B03204.
- Mavko, G., Mukerji, T., and Dvorkin, J., 1998, *The rock physics handbook: tools for seismic analysis in porous media*: Cambridge University Press.
- Nedelec, J.C., 1980, Mixed finite elements in r^3 : *Numer. Math.*, **35**, 315–341.
- Nitsche, J., 1981, On Korn’s second inequality: *RAIRO Anal. Numer.*, **15**, 237–248.
- Norris, A.N., 1993, Low-frequency dispersion and attenuation in partially saturated rocks: *J. Acoust. Soc. Am.*, **94**, 359–370.
- Pride, S.R. and Berryman, J.G., 2003, Linear dynamics of double-porosity and dual-permeability materials. i. governing equations and acoustic attenuation: *Phys. Rev. E*, **68**, 036603.
- Pride, S.R., Berryman, J.G., and Harris, J.M., 2004, Seismic attenuation due to wave-induced flow: *Journal of Geophysical Research*, **109**, B01201.
- Raviart, P.A. and Thomas, J.M., 1975, Mixed finite element method for 2^{nd} order elliptic problems: *Mathematical aspects of the finite element methods, lecture notes of mathematics*, vol. 606: Springer.
- Rubino, J.G., Santos, J.E., Picotti, S., and Carcione, J.M., 2007, Simulation of upscaling effects due to wave-induced fluid flow in Biot media using the finite-element method: *J. Appl. Geophys.*, **62**, 193–203.
- Santos, J.E., Corbero, J.M., Ravazzoli, C.L., and Hensley, J.L., 1992, Reflection and transmission coefficients in fluid-saturated porous media: *J. Acoust. Soc. Am.*, **91**(4), 1911–1923.
- Santos, J.E., Ravazzoli, C.L., Gauzellino, P.M., and Carcione, J.M., 2005, Numerical simulation of ultrasonic waves in reservoir rocks with patchy saturation and fractal petrophysical properties: *Computational Geosciences*, **9**, 1–27.
- White, J.E., 1975, Computed seismic speeds and attenuation in rocks with partial gas saturation: *Geophysics*, **40**, 224–232.
- White, J.E., Mikhaylova, N.G., and Lyakhovitskiy, F.M., 1975, Low-frequency seismic waves

in fluid-saturated layered rocks: *Izvestija Academy of Science USSR. Phys. Solid Earth*, **10**, 654–659.

	Sandstone 1	Sandstone 2	Shale
K_s	37 GPa	37 GPa	25 GPa
ρ_s	2650 Kg/m ³	2650 Kg/m ³	2550 Kg/m ³
ϕ	0.3	0.2	0.3
K_m	4.8 GPa	12.1 GPa	3.3 GPa
μ	5.7 GPa	14.4 GPa	1.2 GPa
κ	1 Darcy	0.23 Darcy	1.5×10^{-5} Darcy

Table 1: Physical properties of the solid materials used in the numerical examples

	Water	Gas
K_f	2.25 GPa	0.012 GPa
ρ_f	1040 Kg/m ³	78 Kg/m ³
η	0.003Pa·s	0.00015 Pa·s

Table 2: Physical properties of the fluids used in the numerical examples

FIGURE CAPTIONS

Figure 1. Schematic representation of an oscillatory compressibility test to estimate the equivalent complex P-wave modulus of a sample.

Figure 2. Schematic representation of an oscillatory shear test to obtain the equivalent complex shear modulus of a sample.

Figure 3. Local degrees of freedom (*dofs*) associated with each component of the solid and the fluid displacement vectors.

Figure 4. P-wave phase velocity obtained from the compressibility test (dots) and using White's theory (line) for frequencies lying between 0 and 100 Hz.

Figure 5. P-wave inverse quality factor obtained from the compressibility test (dots) and using White's theory (line) for frequencies lying between 0 and 100 Hz.

Figure 6. Equivalent shear modulus vs. shale fraction estimated with the shear test and the corresponding values given by the Reuss average in the low-frequency limit.

Figure 7. Gas-water distribution for a given realization. The black zones correspond to pure gas saturation and the white ones to pure water saturation. The overall gas saturation is 0.1.

Figure 8. Normalized fluid-pressure amplitude for the fluid distribution shown in Figure 7. The excitation frequency is 50 Hz.

Figure 9. Averaged variance of compressional phase velocity as a function of the total number of realizations N_R .

Figure 10. Effective compressional phase velocity as a function of the frequency (solid lines). Dotted lines indicate the corresponding standard deviations.

Figure 11. Effective compressional inverse quality factor as a function of frequency (solid lines). Dotted lines indicate the corresponding standard deviations.

Figure 12. Distribution of shale and sandstone for a given realization. The black zones correspond to pure shale and the white ones to pure sandstone.

Figure 13. Effective compressional inverse quality factor as a function of the frequency (solid lines). Dotted lines indicate the corresponding standard deviations.

Figure 14. Normalized fluid-pressure amplitude corresponding to the realization shown in Figure 12 for an excitation frequency of 20 Hz. This field has been truncated in order to see the normalized fluid pressure amplitude in more detail.

Figure 15. Effective shear inverse quality factor as a function of the frequency (solid lines). Dotted lines indicate the corresponding standard deviations.

FIGURES

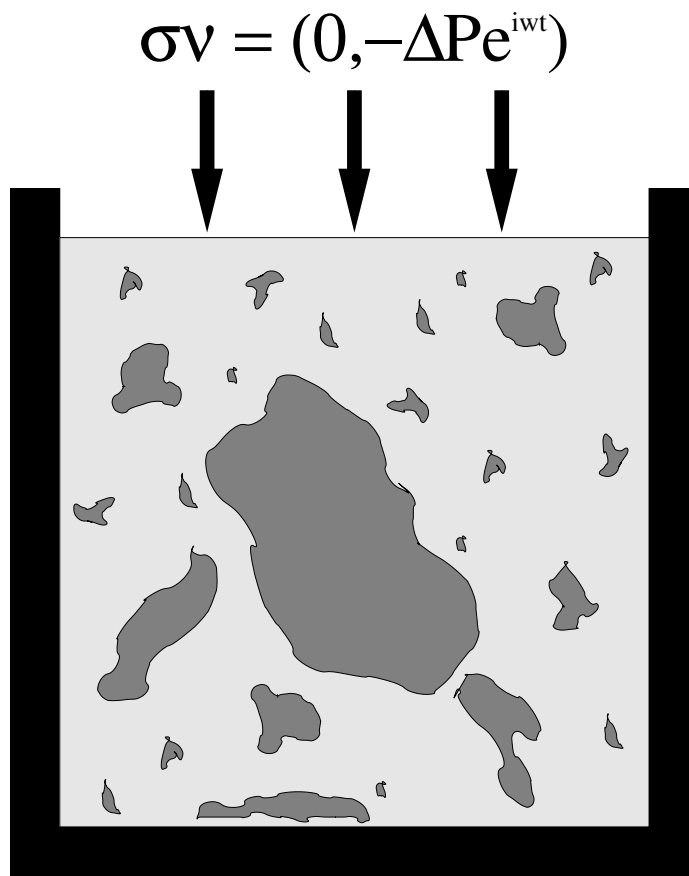


Figure 1:

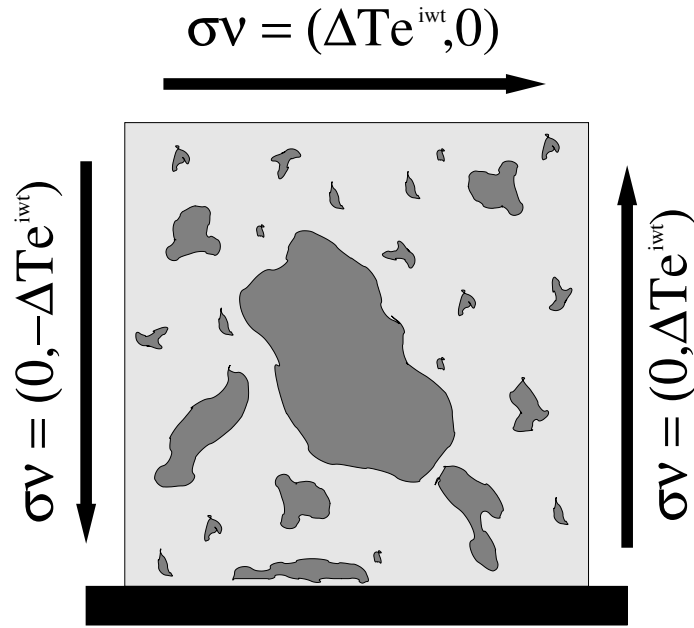


Figure 2:

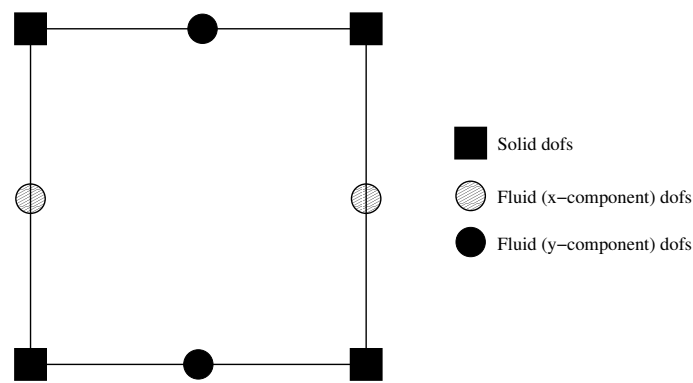


Figure 3:

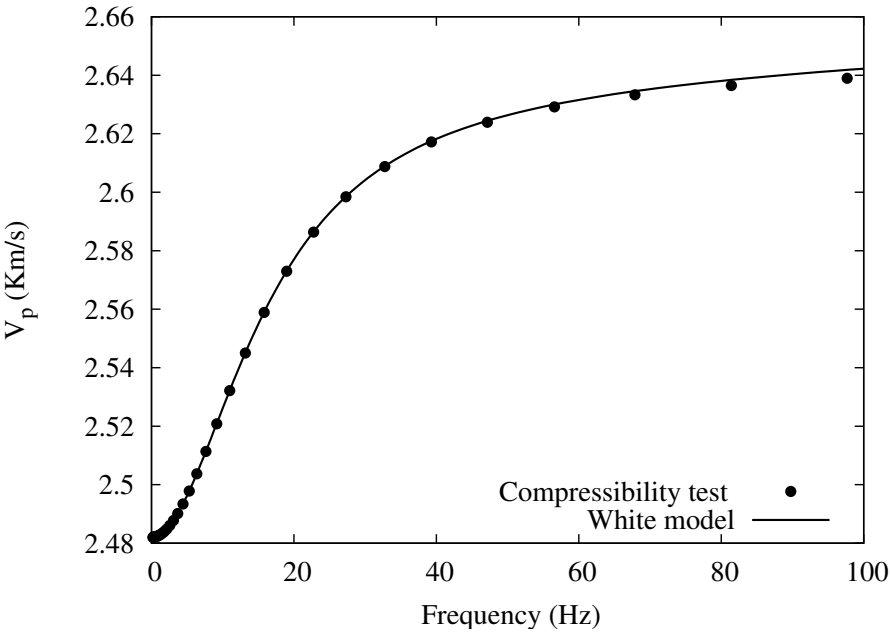


Figure 4:

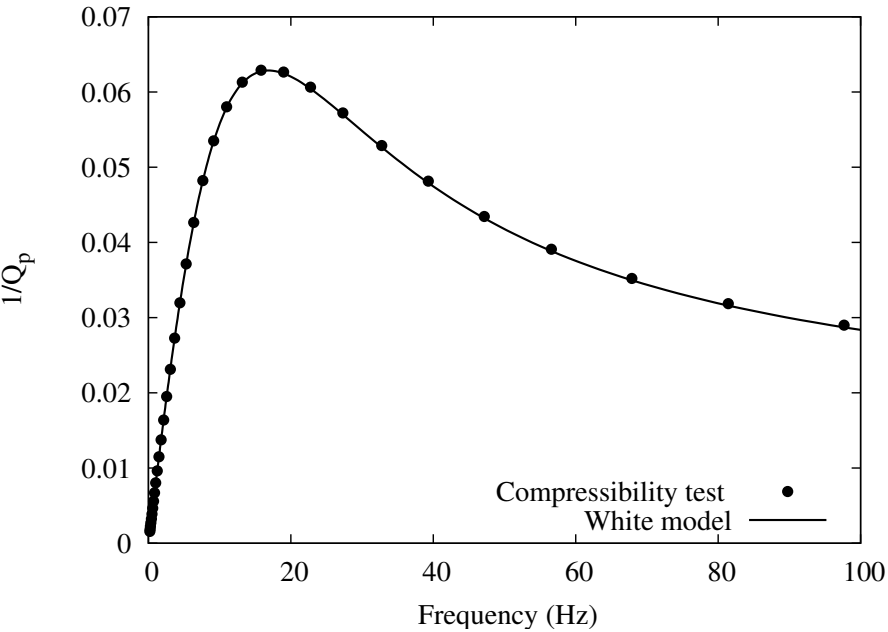


Figure 5:

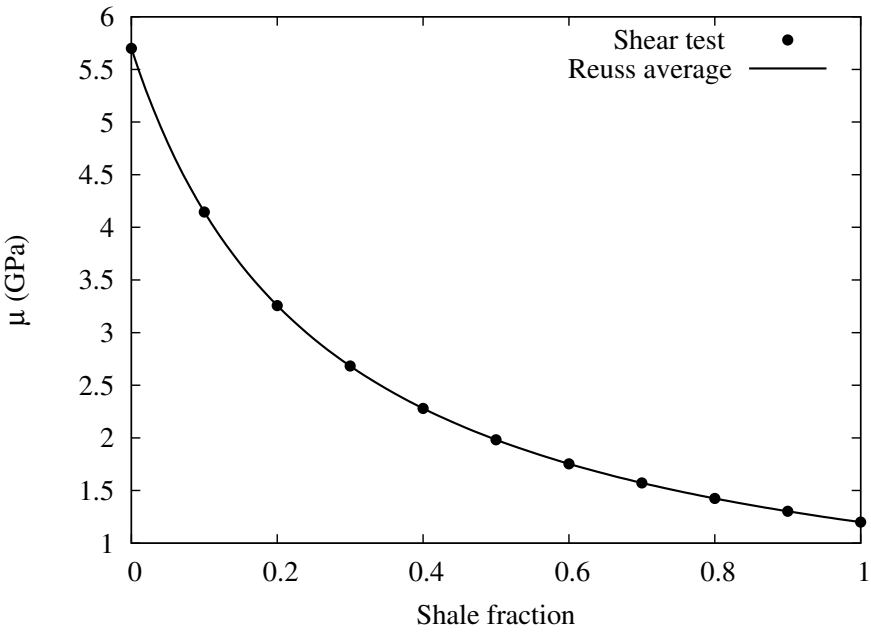


Figure 6:

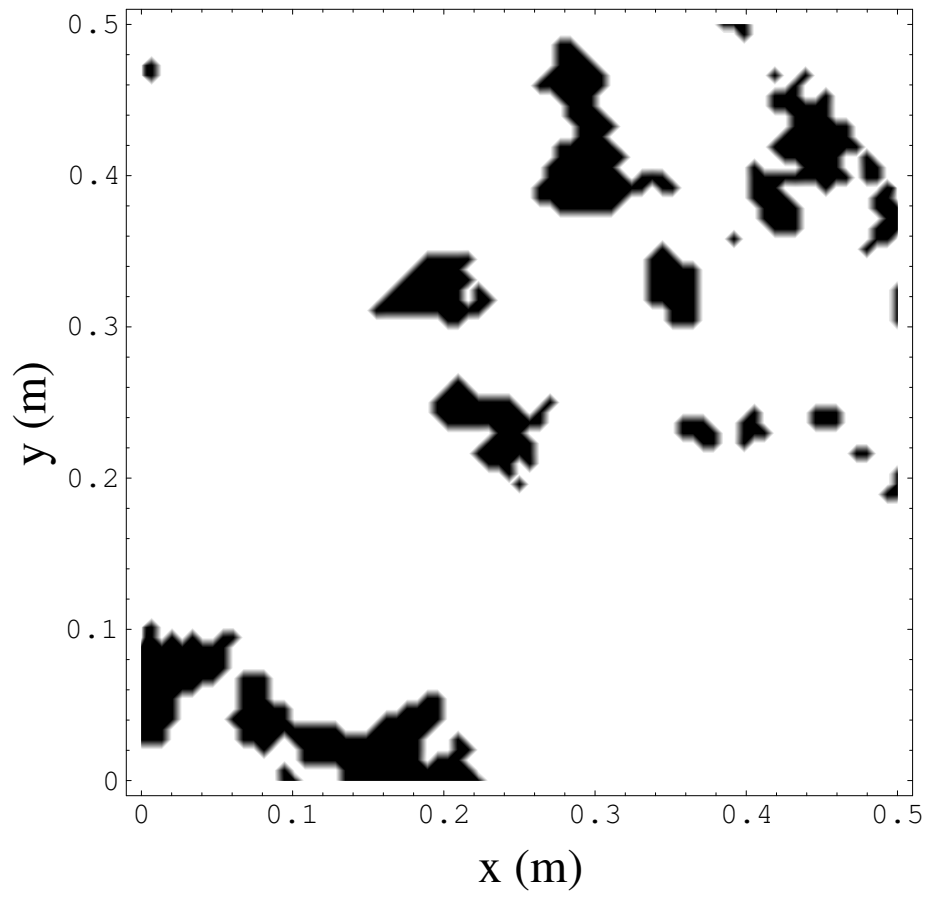


Figure 7:

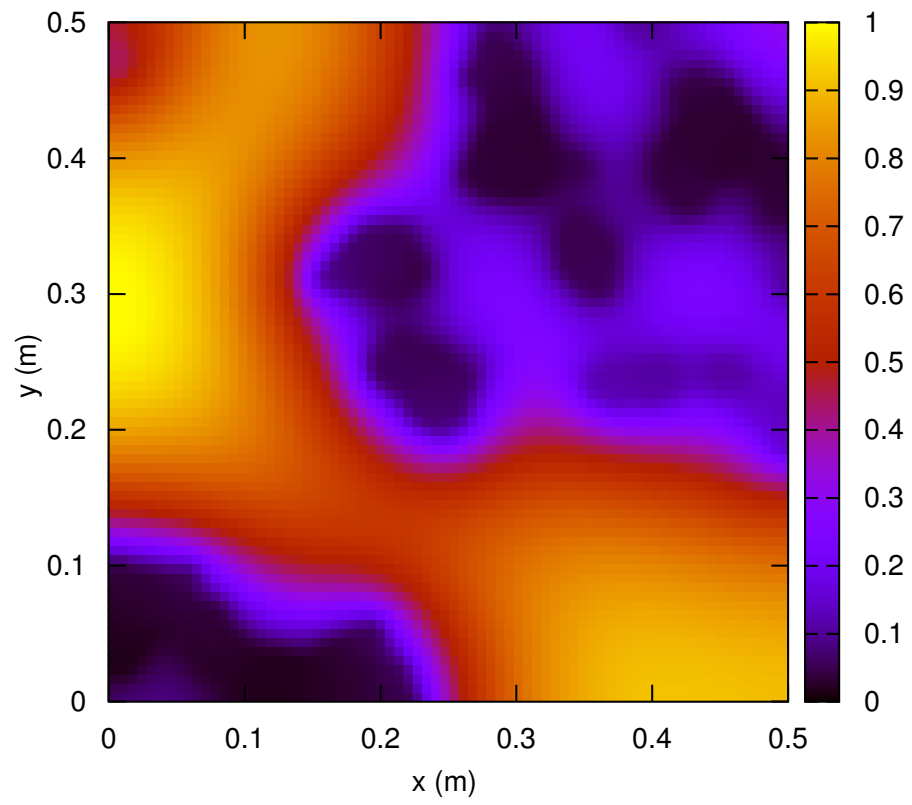


Figure 8:

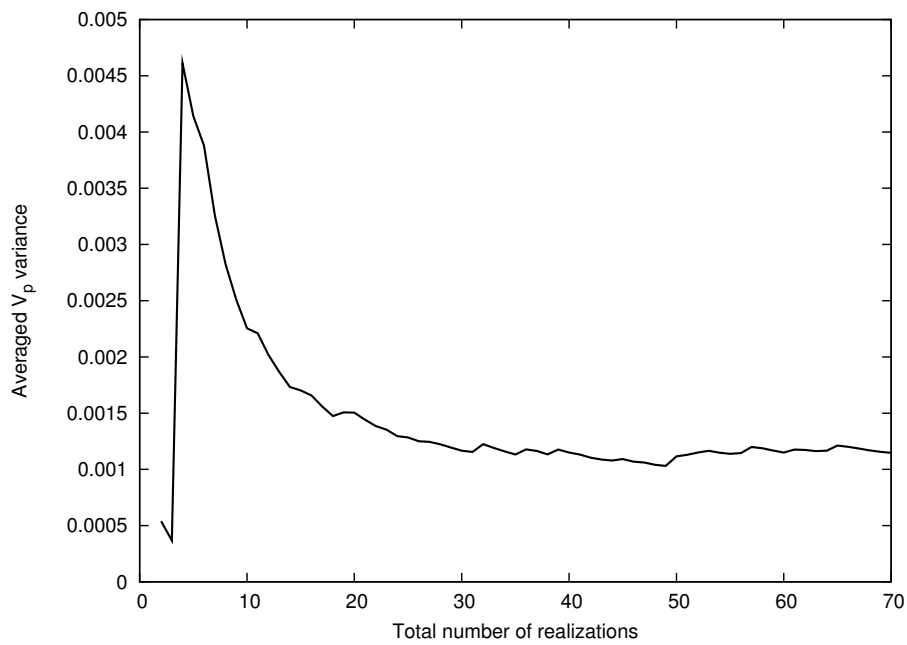


Figure 9:

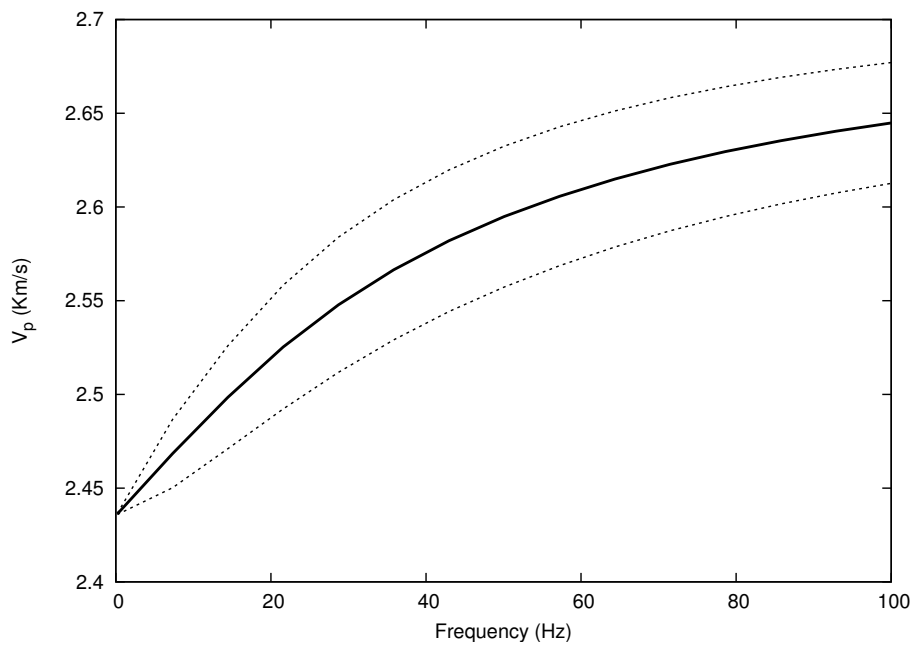


Figure 10:

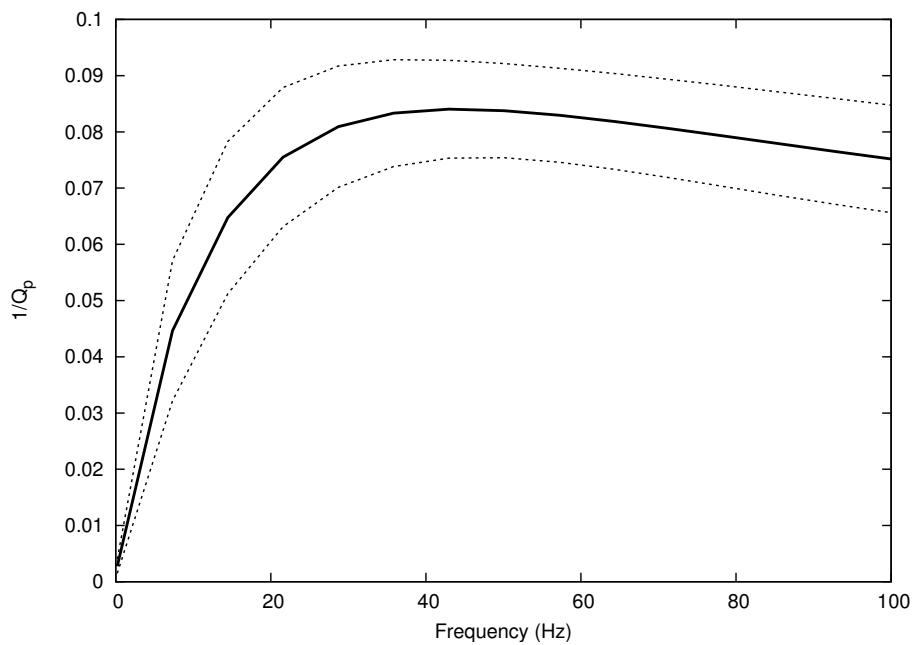


Figure 11:

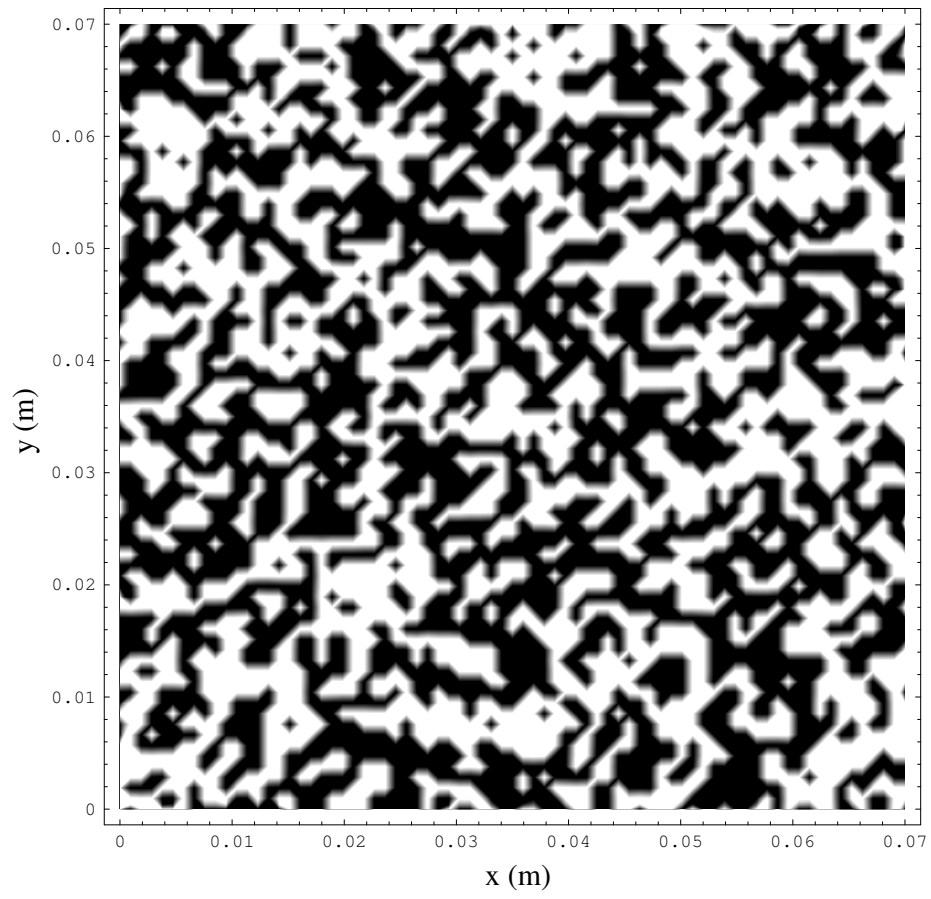


Figure 12:

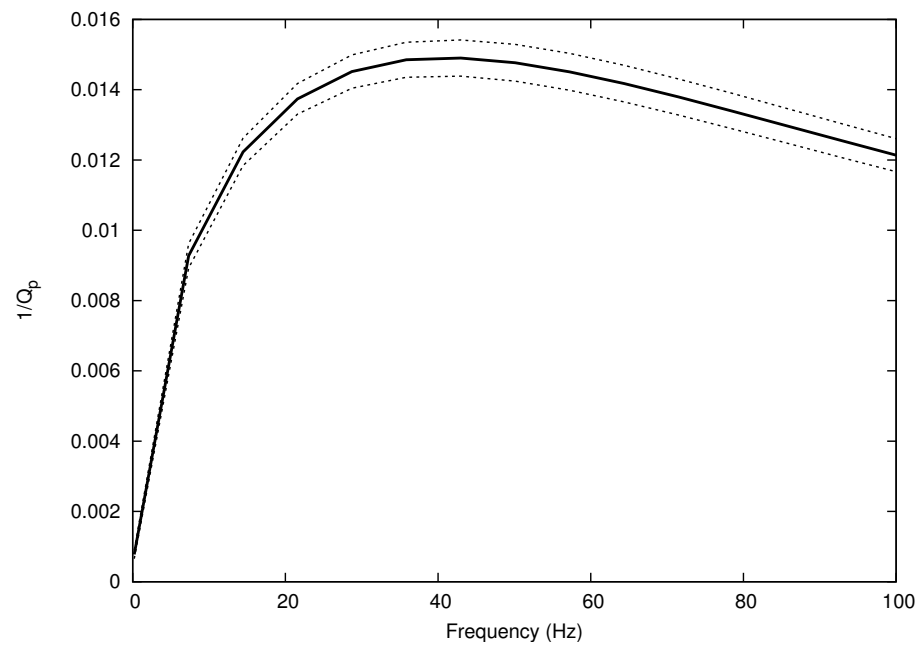


Figure 13:

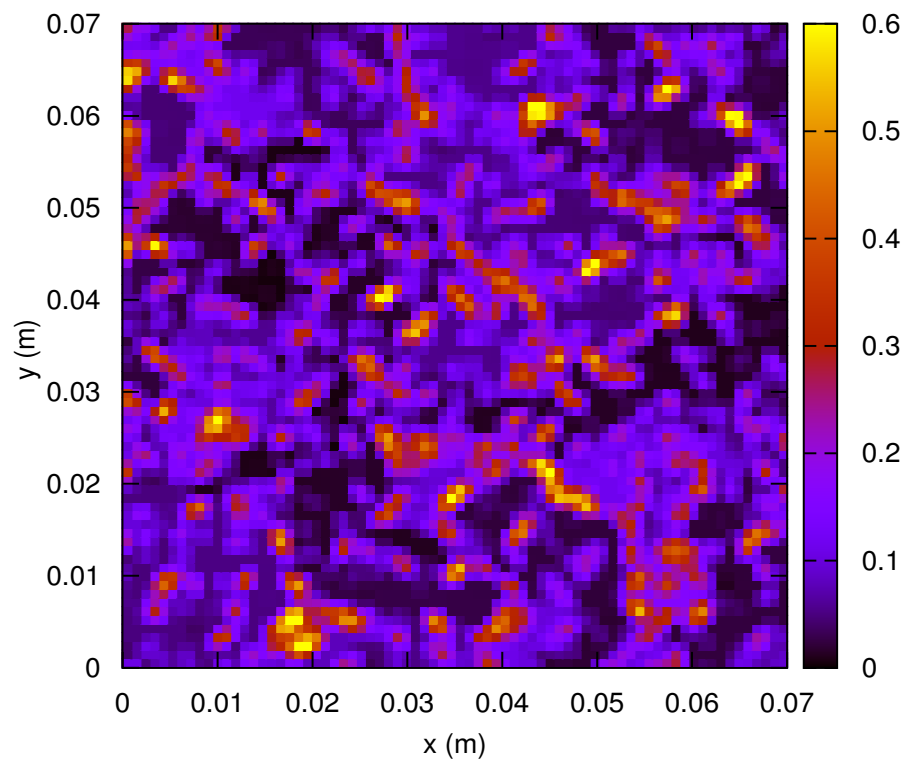


Figure 14:

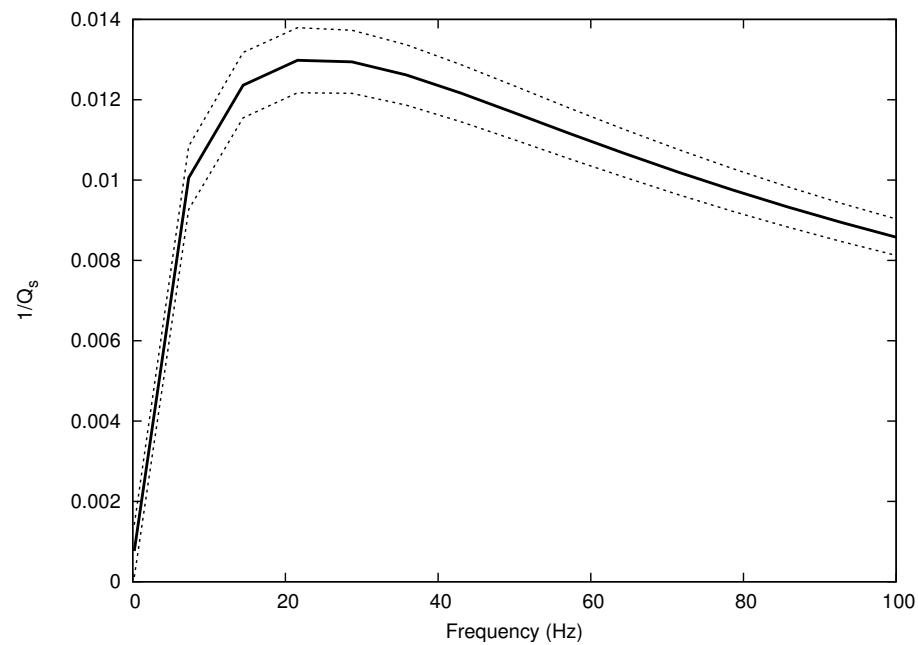


Figure 15: